

Phase-resolved optical emission of dusty rf discharges: Experiment and simulationAndré Melzer,^{1,*} Simon Hübner,^{1,†} Lars Lewerentz,^{1,‡} Konstantin Matyash,^{2,§}
Ralf Schneider,^{1,||} and Ramana Ikkurthi^{3,¶}¹*Institut für Physik, Ernst-Moritz-Arndt-Universität, D-17489 Greifswald, Germany*²*Max-Planck Institut für Plasmaphysik, EURATOM Association, D-17491 Greifswald, Germany*³*Institute for Plasma Research, Bhat, Gandhinagar, Gujarat, India*

(Received 16 November 2010; revised manuscript received 11 January 2011; published 29 March 2011)

The spectral emission of atoms in a dusty radio frequency (rf) discharge plasma in argon and helium has been measured with a gated ICCD camera. The spatially and temporally resolved emission/excitation of the argon and helium atoms during the rf cycle in the dusty discharge was compared to the dust-free case. In the bulk plasma above the dust cloud, the emission is clearly enhanced in the dusty discharge with respect to the pure discharge, whereas in the sheath the emission is reduced. In addition, the emission of a dusty argon plasma is studied via particle-particle particle-mesh (P³M) simulations. The rf dynamics with a single dust particle trapped in the sheath was calculated. Like in the experiment the dust modifies the atomic emission. The spatiotemporal excitation pattern of the experiment is reproduced and a detailed understanding of the difference in excitation of the discharge with and without dust is presented.

DOI: [10.1103/PhysRevE.83.036411](https://doi.org/10.1103/PhysRevE.83.036411)

PACS number(s): 52.27.Lw, 51.50.+v, 52.25.Os

I. INTRODUCTION

Particle-containing (“dusty” or “complex”) plasmas have been studied intensively over the last years with respect to the fascinating properties of dust particles trapped in the gaseous plasma environment. Extensive investigations have covered, e.g., crystal formation, phase transitions, and wave activities, but also particle charging, forces on the particles, and much more (see, e.g., Refs. [1–3] for an overview).

Not only are the particles affected by the plasma, but naturally also the plasma reacts to the presence of the dust particles. Effects that have been discussed include, among others, electron depletion due to particle charging (see, e.g., [4,5]), the change of electrical properties of the dusty plasma discharge (see, e.g., [6–8]), and the increase of electron temperature due to additional plasma losses on the dust (see, e.g., [9–11]).

Spectroscopic investigations of dusty plasmas allow the extraction of discharge properties with high spatial and temporal resolution. For example, Bouchoule *et al.* [7] have deduced an increase of metastable density due to the global increase of electron energy from the investigation of specific argon lines. Further, the density of different excited states of argon have been measured by Mitic *et al.* [12] by self-absorption methods. Moreover, loss of metastables on the particles in a dust cloud has been observed by laser absorption spectroscopy in a neon discharge by Do *et al.* [13]. In a recent experiment, we have studied the spatiotemporal evolution of the emission in the sheath of an argon discharge using a gated and intensified charge-coupled device (ICCD) camera [14]. There, we were

able to measure the phase-resolved emission during the rf cycle. For one specific argon line, we have observed an increase of plasma emission with small dust particles and a decrease of emission with large particles in a relatively small dust cloud.

Plasma emission allows a local approach to the plasma properties since the emission can be studied even in the plasma sheath where the highly nonequilibrium environment complicates other diagnostic methods. Using fast gated cameras, the plasma emission can be resolved within the rf cycle of a standard rf discharge.

Here, we will address the question of the influence of the dust on the plasma discharge properties by phase-resolved optical emission spectroscopy. In contrast to the previous experiment [14] large dust clouds are studied and the investigations are extended to the behavior of several different emission lines in argon and helium discharges.

In order to elucidate the experimental results a particle-particle particle-mesh (P³M) simulation [15–17] is used to model capacitively coupled radio frequency (CCRF) discharges with and without dust. The results of the difference in excitation are compared and validated with the experimental results. The aim of this work is to gain further insight into the mechanism of increased excitation above the dust.

After a description of the experiment and the P³M code, we discuss the experimental results for the spatiotemporal excitation patterns in dusty and dust-free discharges for different emission lines. Afterward the modeling results using the P³M code for phase-resolved dynamics in dusty rf discharges are presented. The effect of a single dust particle and its influence on the CCRF plasma are discussed. Finally, the major findings are summarized.

II. EXPERIMENT

The experiments have been performed in a capacitively coupled rf discharge between parallel plates, see Fig. 1. The discharge was operated in argon or helium at 13.56 MHz at various rf powers between 5 and 40 W and gas pressures between 5 and 40 Pa. Different types of monodisperse plastic

*melzer@physik.uni-greifswald.de

†Present address: Department of Applied Physics, Technical University Eindhoven, NL-5600 MB Eindhoven, The Netherlands.

‡lleweren@ipp.mpg.de

§knm@ipp.mpg.de

||schneider@uni-greifswald.de

¶ramana468@gmail.com

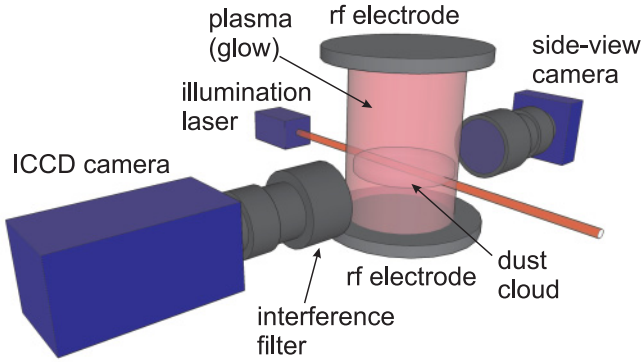


FIG. 1. (Color online) Scheme of the setup. See text for details.

microspheres with diameters ranging between $2a = 2.5 \mu\text{m}$ and $2a = 12 \mu\text{m}$ have been used in the experiments (a is the particle radius). The microspheres have been dropped into the discharge where the particles are trapped in the sheath above the lower electrode by a balance of electric field force and gravity. In the sheath, the particles arrange in a flat cloud of about 1 mm thickness; horizontally the dust cloud is confined by a circular barrier of 12 cm diameter. Thus, the dust cloud floats above almost the entire electrode area. Before and after the emission measurements, the dust cloud was observed from the side by a video camera to monitor the vertical position of the cloud.

The dust density in the dust cloud was $n_d = (4 \pm 1) \times 10^{11} \text{ m}^{-3}$ and $n_d = (1.2 \pm 0.4) \times 10^{11} \text{ m}^{-3}$ for the preferably used particles of 3.5 and 10 μm , respectively. Taking a floating potential on the dust of -3.1 V (see Sec. V A) and assuming a linear dependence of dust charge on radius (as suggested by OML theory) in both cases a similar charge density $Z_d n_d = 1.4 \times 10^{15} \text{ m}^{-3}$ is obtained which is close to the electron charge density in this discharge (see Sec. IV C). Hence, the experiments have been performed at roughly the same dust charge densities.

To measure the time and space resolved emission, we have applied phase-resolved optical emission spectroscopy, see, e.g., [18–20] and references therein. An ICCD (Princeton Instruments PI-Max2) camera imaged the discharge directly above the lower electrode. With a lens system the central part of

TABLE I. Investigated emission lines in argon and helium together with the respective transitions (in Paschen’s notation for argon), the lifetimes, and the applied filter wavelengths. Data from Refs. [21,22].

Wavelength	Transition	Lifetime τ	Filter
Ar 750.4 nm	$2p_1 \rightarrow 1s_2$	22.5 ns	750 nm
Ar 751.5 nm	$2p_5 \rightarrow 1s_4$	24.9 ns	750 nm
Ar 810.3 nm	$2p_7 \rightarrow 1s_4$	40.0 ns	810 nm
Ar 811.5 nm	$2p_9 \rightarrow 1s_5$	30.2 ns	810 nm
Ar 840.8 nm	$2p_3 \rightarrow 1s_2$	44.8 ns	840 nm
Ar 842.5 nm	$2p_8 \rightarrow 1s_4$	46.5 ns	840 nm
He 587.5 nm	$2^3P \rightarrow 3^3D$	34.0 ns	589 nm
He 667.8 nm	$2^1P \rightarrow 3^1D$	15.7 ns	670 nm

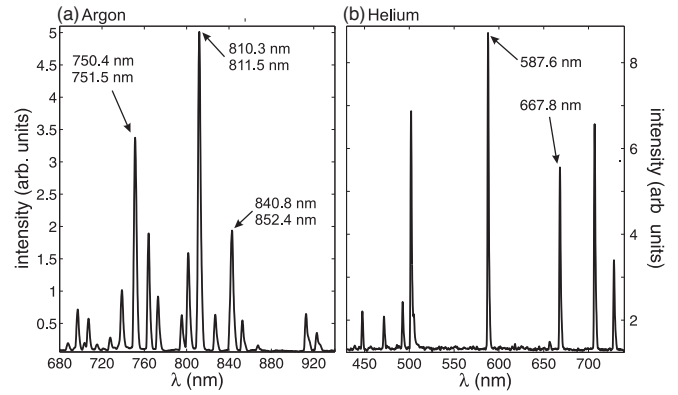


FIG. 2. Spectral intensities of (a) the argon and (b) the helium discharge. The investigated lines are indicated.

the electrode and the sheath above the electrode were focused to the camera chip. The discharge area viewed by the camera was approximately $20 \times 20 \text{ mm}^2$.

The ICCD camera was gated at 5 ns time windows triggered from the rf generator. By changing the delay between the trigger and the 5 ns window in steps of 2 ns the complete rf cycle ($T_{\text{rf}} = 74 \text{ ns}$) was measured. For each delay setting, the light arriving at the ICCD in the 5 ns window was accumulated over 6000 cycles. For the helium discharges it was necessary to increase the gating time to 10 ns for adequate intensities. For the data presented here, the emission in the $20 \times 20 \text{ mm}^2$ area was averaged over the horizontal coordinate. Thus, we have obtained a vertical emission profile that contains the emission within 5 ns or 10 ns (averaged over 6000 cycles) in 2 ns steps.

The camera was equipped with an interference filter to select specific argon and helium emission lines. The spectral lines observed in helium and argon are listed in Table I together with their lifetimes and the applied interference filter wavelengths. The filters have a typical uncertainty in the central wavelength of about 1 nm and a FWHM of 10 nm. In argon, due to this limited bandwidth, typically the emission from two different lines is recorded simultaneously. With the filter at 750 nm, the emission from the argon lines at 750.4 and 751.5 nm is recorded. The 810 nm filter includes the lines at 810.3 and 811.5 nm, that at 840 nm includes 840.8 and 842.5 nm. Most of the results presented here have been obtained with the 750 nm filter.

Typical spectra of the helium and argon discharges are shown in Fig. 2. The selected lines are among the most intense lines and those with the shortest lifetimes in order to favor an observable intensity variation within the rf cycle.

III. SIMULATION

The particle-in-cell (PIC) method with Monte Carlo collisions (MCC) has proven to be a powerful tool for the description of rf discharges. Especially, it is able to resolve the spatiotemporal excitation patterns for various gases in the nonequilibrium nonstationary environment of rf discharges [15,23,24]. For the study of small dust particles in a plasma, the ordinary PIC scheme has one considerable drawback: Space resolution of the PIC method is limited to the grid size, typically of the order of a Debye length. Particles in

PIC are represented by charged clouds, which are distributed over the grid size. This allows particles to penetrate each other [25], leading to high inaccuracies of the interparticle interaction when the distance becomes smaller than the cell size. Therefore, the interaction force strongly deviates from the Coulomb force for small distances and tends to go to zero as the interparticle distance decreases [17]. Dust grains used in laboratory experiments are typically much smaller than such a cell (nano- or micrometers in size). In order to resolve close-range interactions between dust grains and plasma particles accurately, a particle-particle particle-mesh (P³M) model was used. For details of the model see [16]. This technique combines a PIC-MCC model with the molecular dynamics (MD) approach in order to calculate the background plasma and to resolve finite-size effects of dust particles correctly. The interaction force between the dust grain and plasma particles, which are within a certain distance (about a Debye length) to the dust grain, is computed according to a direct particle-particle MD scheme. Since the dust contribution $E_{\text{grid,dust}}$ already is accounted for in the electric field E_{grid} of the PIC part, it is replaced by a direct particle-particle scheme using exact Coulomb electric field E_{Coulomb} . The resulting electrostatic field in the vicinity of the dust particle is thus calculated as: $E = E_{\text{grid}} - E_{\text{grid,dust}} + E_{\text{Coulomb}}$. Due to the fact that plasma particle motion occurs on scales of the dust grain size, plasma particles in the MD region need to be moved with smaller time step than in ordinary PIC. If plasma particles in the simulation approach dust coordinates closer than the radius of the dust grain they are counted as absorbed, no additional surface effects are considered, and their charge is added to the dust charge. By considering finite-size effects, this method allows us to follow plasma particle trajectories in the vicinity of the dust particle. Thus, the charging of dust due to absorption of electrons and ions is resolved self-consistently.

To mimic the experimental conditions, argon was modeled as the working gas in a parallel plate capacitor. Initially, electron density and temperature were chosen as $n_{e,0} = 10^{15} \text{ m}^{-3}$ and $T_{e0} = 2.5 \text{ eV}$, respectively. The neutral gas temperature was fixed to 300 K at a pressure of 50 Pa. The frequency of the rf was set to $\omega_{\text{rf}} = 13.56 \text{ MHz}$. Since the neutral gas density was much higher than the densities of the charged constituents, only the dynamics of charges was followed and the neutral gas was treated as a background with fixed density n_{Ar} and temperature. Given the parameters above, the calculation resulted in an electron plasma frequency $\omega_{pe} = 1.8 \text{ GHz}$ and a electron Debye length $\lambda_{De} = 372 \mu\text{m}$. Hence, a time step $\Delta t = 0.2/\omega_{pe} = 1.12 \times 10^{-10} \text{ s}$ and grid spacing $\Delta x = 0.5\lambda_{De}$ have been used in the simulation.

The motion was resolved in three dimensions in space and velocity (3D3V). The computational domain was split into $8 \times 128 \times 8$ PIC cells in the x , y , and z directions, respectively. This corresponded to a discharge of volume $1.5 \text{ mm} \times 24 \text{ mm} \times 1.5 \text{ mm}$. In the y direction the domain was limited by ideally absorbing electrodes. The lower electrode at $y = 0 \text{ mm}$ was driven by a sinusoidal voltage $U_{\text{rf}} = U_0 \sin(\omega_{\text{rf}}t + \varphi)$ with an amplitude of $U_0 = 50 \text{ V}$ and phase φ . The upper electrode at $y = 24 \text{ mm}$ was grounded. In the x and z directions the domain was periodic and particles were reinjected with proper momentum and position. After a transient phase the model reaches a dynamic equilibrium of the simulated discharge.

Electron temperature and density converged to $T_{e0} = 3.4 \text{ eV}$ and $n_{e,0} = 7.5 \times 10^{14} \text{ m}^{-3}$, respectively (compare to Sec. IV C for experimental results at slightly higher voltage).

In experiments dust particles levitate in the sheath above the lower electrode, where gravity is balanced by the electric force exerted on the dust. The time scales of the dust particle motion are much larger than the dynamics of the rf. Therefore, after equilibration of the plasma background a dust particle with $10 \mu\text{m}$ diameter is added to the domain. It is at a fixed position within the sheath at $y = 4.4 \text{ mm}$ above the lower electrode.

Coulomb collisions between charged species as well as inelastic collisions such as ionization, excitation, and charge exchange have been considered. The plasma was sustained self-consistently due to electron impact ionization of the neutrals by electrons accelerated in the rf sheaths.

For the comparison with the experiment the spatiotemporally resolved excitation rates have been calculated for several argon lines. The ground state of argon has an electron configuration of $1s^2 2s^2 2p^6 3s^2 3p^6$. The first lowest excited levels arise from the $3p^5 4s$ configuration. In Paschen's notation they are labeled as the $1s_2$ to $1s_5$ levels. Next excited states arise in the p level, called $2p_1$ to $2p_{10}$ [21,26]. In this simulation only the transition from $2p_1$ to $1s_2$ at a wavelength of 750.4 nm is considered. The excitation rate was calculated as

$$R = n_{\text{Ar}} \int_0^{v_{\text{max}}} \sigma(E) f_e(v) v_{\text{rel}} 4\pi v^2 dv, \quad (1)$$

where f_e is the electron velocity distribution function calculated with the P³M model. Thus, the emission intensity (and thus the excitation) decisively depends on the local electron density and the electron distribution function. Since the electrons are much more mobile, neutrals can be assumed as fixed. The relative velocity v_{rel} between argon neutrals and electrons can be approximated by the electron velocity $v_{\text{rel}} \approx v$. It was assumed that excitation of the $2p_1$ argon state appeared from ground state. This transition has a threshold energy $E_{\text{exc}} = 13.47 \text{ eV}$. A total (direct and cascade) electron impact excitation cross section $\sigma(E)$ can be found in [27,28].

IV. EXPERIMENTAL RESULTS

Beginning with the experiments, we start with a description of the emission and excitation pattern. Afterward we will address the dust-induced differences on the atomic excitation in the discharge.

A. Spatiotemporal emission and excitation

First, the space and time resolved emission of the two argon lines observed with the 750 nm filter is shown in Fig. 3 for a discharge at a discharge power of 20 W and a gas pressure of 30 Pa for the cases with and without trapped dust. One clearly sees that the emission is modulated at the frequency of the rf discharge. The emission has its maximum when the sheath is expanding and slowly reduces over the remaining rf cycle (the corresponding rf voltage is shown in the upper panel of Fig. 4). Such a behavior is well known (see, e.g., Refs. [18–20] and references therein) and it is typical for discharges in noble gases [29]. Vertically (denoted by the coordinate z), the

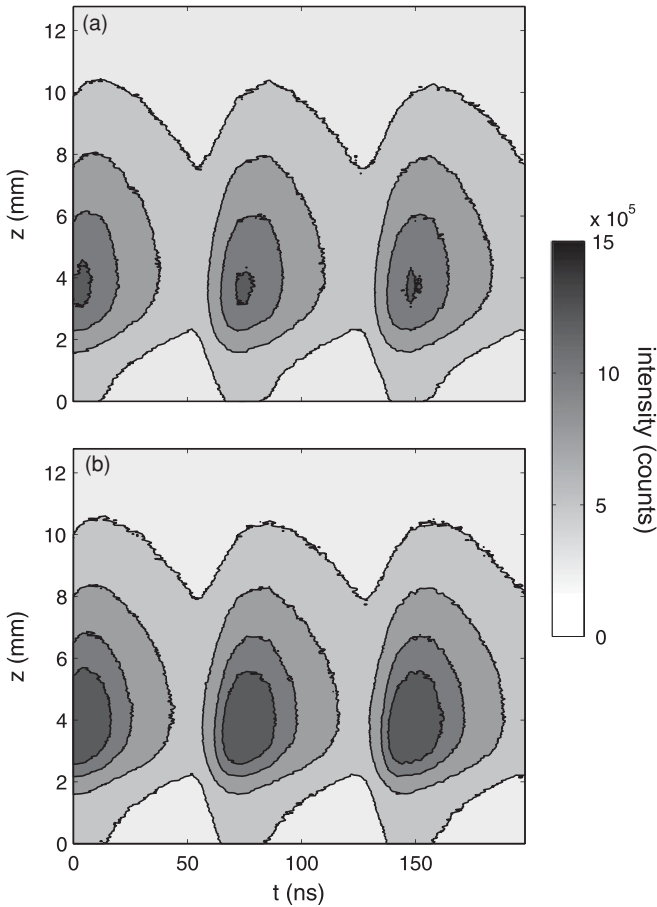


FIG. 3. Measured spatiotemporally resolved emission at 750 nm of the argon discharge (a) without and (b) with $10\ \mu\text{m}$ dust trapped in the sheath. The temporal axis covers 200 ns corresponding to nearly 3 rf cycles.

maximum intensity is found somewhat below 4 mm above the lower electrode in line with previous investigations [30,31].

Taking the dust-free situation in Fig. 3(a) as the reference we now compare it to the particle-containing case in Fig. 3(b), where microspheres of $10\ \mu\text{m}$ diameter are trapped in the sheath of the discharge. One sees a very similar emission pattern for the dust case. However, the maximum emission intensity in the dust case is increased with respect to the dust-free case. This can already be taken as a hint toward higher electron energies when dust is present.

Rather than studying the emission it is often more instructive to address the excitation pattern, especially for comparison with numerical modeling. The excitation is reconstructed from the emission by accounting for the finite lifetime of the transitions τ . The excitation $X_{\text{exc}}(t)$ is obtained via the relation

$$X_{\text{exc}}(z,t) \propto \frac{dI(z,t)}{dt} + \frac{I(z,t)}{\tau}, \quad (2)$$

where $I(z,t)$ is the measured spatially and temporally resolved emission intensity. Figure 4 shows the excitation for the dust-containing case of Fig. 3(b). The excitation is deconvoluted from the emission using a mean lifetime of $\tau = 23\ \text{ns}$ for the two argon lines at 750 nm and a numerical differentiation for $dI(z,t)/dt$. As expected [29], the excitation pattern is more concentrated in a shorter time period and it is clearly in the

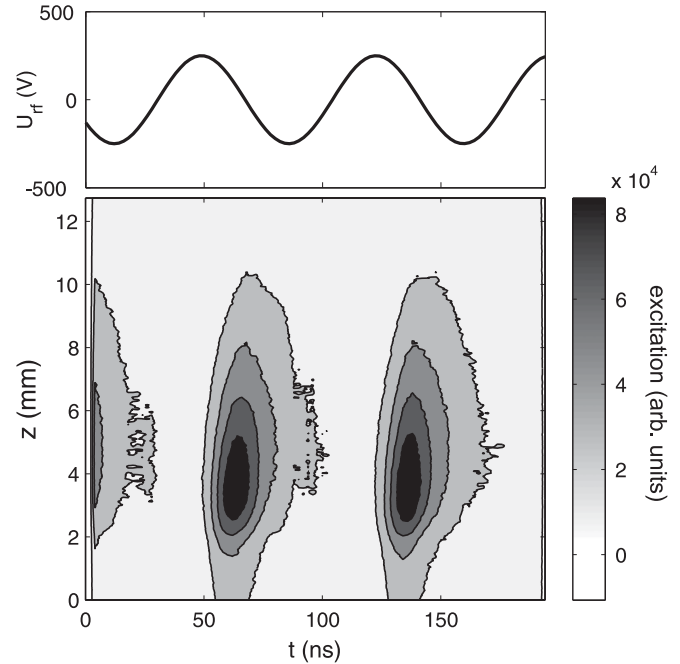


FIG. 4. Spatiotemporal excitation of the 750 nm spectral line with $10\ \mu\text{m}$ dust trapped in the sheath derived from the deconvolution of the emission [see Fig. 3(b)]. The upper panel shows the rf voltage applied to the lower electrode.

expansion phase of the rf sheath when the voltage at the lower electrode drops from its maximum value toward its minimum (the excitation pattern is slightly shifted to earlier times by about 10 ns by deconvolution). In the following, we will mainly refer to the excitation patterns.

B. Comparison of dusty and dust-free discharges

To illustrate the influence of the dust trapped in the sheath we now compare the excitation with trapped dust $X_{\text{exc},d}(z,t)$ and without dust $X_{\text{exc},0}(z,t)$. Figures 5 and 6 show the difference of these excitation patterns, i.e., $X_{\text{exc},d}(z,t) - X_{\text{exc},0}(z,t)$, calculated for each position and time. The excitation difference is normalized here to the overall maximum value of the excitation without dust.

Figures 5 and 6 show the excitation difference for argon and helium discharges, respectively. In both cases we have varied the diameter of the trapped dust and results are shown for particles of $3.5\ \mu\text{m}$ and $10\ \mu\text{m}$ diameter.

Starting with the situation in argon the excitation of the two spectral lines near 750 nm is found to be strongly affected by $10\ \mu\text{m}$ dust [Fig. 5(b)]. There, one sees an enhanced excitation difference with dust (red areas) at the instant when the absolute excitation is strongest, i.e., when the sheath is expanding. The excitation with dust exceeds that without dust by more than 20%. During sheath collapse the excitation with dust is the same as without dust. However, the strongest effects are seen at $2.5\ \text{mm} < z < 7\ \text{mm}$, i.e., decisively above the dust cloud, which is trapped between $z = 1$ and $2\ \text{mm}$. On this color scale plot, an influence directly at the position of the dust cannot be identified.

For the $3.5\ \mu\text{m}$ dust [Fig. 5(a)] the overall effect is smaller than in the case of $10\ \mu\text{m}$ dust (note the different color

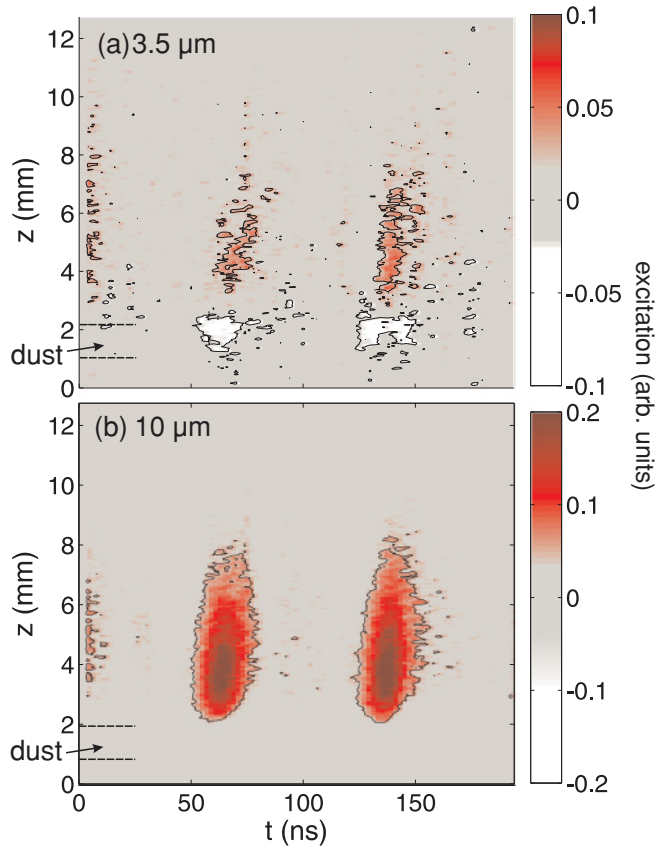


FIG. 5. (Color online) Difference of the excitation of the argon 750 nm lines with dust and without dust. The dust trapped in the sheath has a diameter of (a) $3.5 \mu\text{m}$ and (b) $10 \mu\text{m}$. The difference has been normalized to the maximum value of the excitation in the dust-free case. The height where the dust is trapped is indicated by the horizontal dashed lines.

scale). However, one easily sees enhanced emission above the trapped dust during sheath expansion amounting to 5% to 10% excitation increase. Moreover, at the same instant of time a decrease of the excitation is observed in the height of the trapped dust. This decrease is also of the order of 5% to 10%. Hence, generally, excitation is considerably affected by the dust sheath indicating that the global discharge characteristics are changed by the dust trapped in the sheath.

Turning now to the helium discharge, one sees similar effects. For the $10 \mu\text{m}$ dust [Fig. 6(b)] the excitation of the 667.8 nm spectral line is strongly affected by the dust with an increase of excitation by more than 10% during sheath expansion. The dust effects in helium are therefore somewhat smaller than in argon. Similar to argon, the strongest effects are seen again above the dust cloud at $4 \text{ mm} < z < 10 \text{ mm}$. In the dust cloud ($2.5 \text{ mm} < z < 3.5 \text{ mm}$) the excitation is reduced by about 5% to 10%.

For the $3.5 \mu\text{m}$ particles [Fig. 6(a)] the discharge is affected very weakly. Again, in the dust cloud the excitation is slightly reduced and above the dust cloud a weak increased excitation might be seen. The excitation differences are, as in the case of argon, generally smaller for the $3.5 \mu\text{m}$ dust compared to the $10 \mu\text{m}$ dust. Although the effect for the $3.5 \mu\text{m}$ particles in helium is quite weak the above mentioned general trends can be identified.

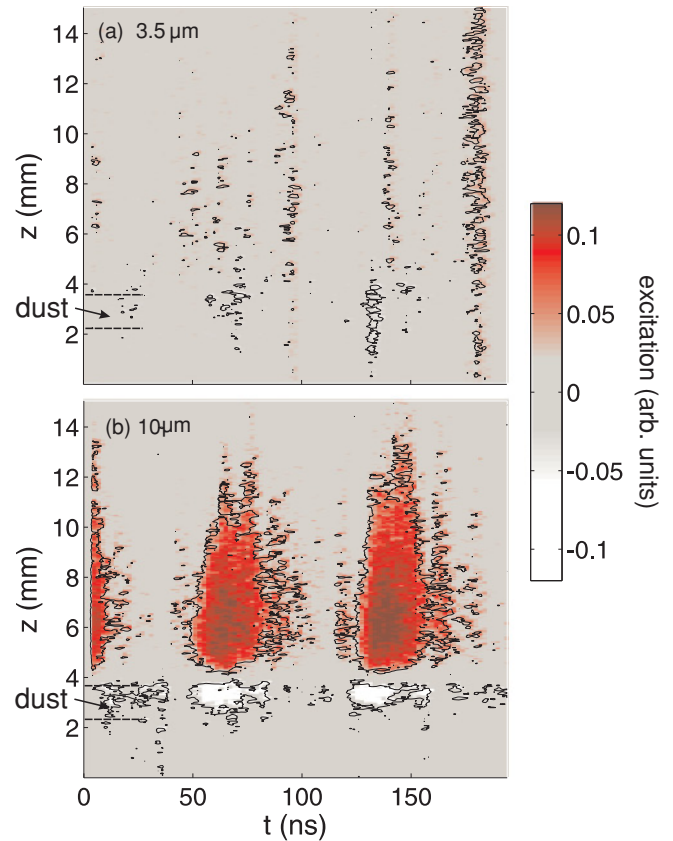


FIG. 6. (Color online) Difference of the excitation of the helium 667.8 nm lines with dust and without dust. The dust trapped in the sheath has a diameter of (a) $3.5 \mu\text{m}$ and (b) $10 \mu\text{m}$. The difference has been normalized to the maximum value of the excitation in the dust-free case. The height where the dust is trapped is indicated by the horizontal dashed lines.

The experiments have been performed at constant power at the rf generator. Since a significant fraction of the rf power is typically dissipated in the matching network an increased emission might be due to different rf power dissipated in the plasma. Therefore, we have monitored the rf voltage as well as the current to the powered electrode for both dusty and dust-free discharges. The current and voltage amplitudes as well as the relative phase varied much less than the emission difference of 20%. We therefore judge that the power delivered to the plasma is nearly the same for dusty and dust-free discharges and that the observed increased emission is not due to an increase of rf power dissipated in the plasma. Further, the fact that the enhanced emission is observed only in a certain part of the rf period (during sheath expansion) and only in a marked spatial region above the dust cloud (but not in the sheath) supports that the plasma power is not generally increased for the dust-containing discharges.

In a previous investigation [14] we have experimentally observed similar phenomena of dust-affected differences in plasma emission. There, similarly as described above, we observed an increase of plasma emission in the plasma volume above the dust cloud when using $3.5 \mu\text{m}$ dust. However, for particles of $10 \mu\text{m}$ a decrease of the plasma emission was seen not only where the dust is trapped, but also in the plasma volume. This is in certain contrast to the findings

here. The main difference between the previous experiment and this one is that here the dust cloud is laterally much larger (12 cm diameter) and covers almost the entire electrode. In the previous experiment the dust cloud diameter was only about 5 cm. Hence, in the experiment here, the dust influence is much more severe, since almost no part of the electrode area is freely exposed to the plasma volume, and the sheath everywhere above the electrode contains particles. In the previous experiment, the unaffected electrode areas could maintain a “normal,” undisturbed plasma operation so that the global discharge parameters were more strongly determined by the unaffected electrode areas. We suspect that the coverage of the entire electrode in this experiment leads to stronger electron heating since the plasma losses on the dust cannot be compensated above the uncovered electrode areas. Consequently, we also observe additional emission above the dust cloud even for the larger particles. This reasoning is supported by the fact that the relative excitation difference is smaller in the previous experiments (5%–10% of maximum emission) than in these experiments (10%–20% of maximum excitation).

C. Time-averaged behavior

To reveal the spatial behavior in more detail, especially in the plasma sheath, we now look at the time-averaged excitation. We therefore have normalized the time-averaged excitation with dust to that without dust for each height above the electrode (note that in Figs. 5 and 6 the excitation was normalized to the global excitation maximum). Hence, this relative excitation is calculated as

$$\bar{X}_{\text{exc}}(z) = \frac{\langle X_{\text{exc},d}(z,t) \rangle_t}{\langle X_{\text{exc},0}(z,t) \rangle_t}, \quad (3)$$

where $\langle \cdot \rangle_t$ indicates averaging over time (at each individual height z).

This relative excitation $\bar{X}_{\text{exc}}(z)$ is shown in Fig. 7 for argon and helium, respectively, using 3.5 and 10 μm particles. At heights above the trapped dust a clear increase of the (mean) plasma excitation is seen. This effect is more pronounced using larger dust particles. In the sheath, however, at positions where the dust is trapped a clear decrease of excitation is observed. This is seen in both argon and helium discharges for both 3.5 and 10 μm particles. Even in the case of 10 μm and argon where the spatiotemporal pattern [Fig. 5(b)] was indifferent, in the position-dependent normalization of Fig. 7(a) a clear dip of excitation is found. This dip might simply be attributed to shadowing by the dust cloud. Similarly, for the 3.5 μm particles in helium, where Fig. 6(a) was very faint, the excitation dip in the sheath and the increased excitation above the dust cloud are observable.

Hence, the effect of the dust on the plasma excitation is twofold. The dust leads to a general increase of plasma excitation in the plasma volume above the dust, but to a (smaller) decrease of plasma excitation in the sheath at positions where the dust is trapped. Both effects seem generally more pronounced for larger dust particles.

In previous simulations [10] and experiments [11] it has been shown that the electron distribution function is affected by the presence of dust. Hence, a modification of the plasma

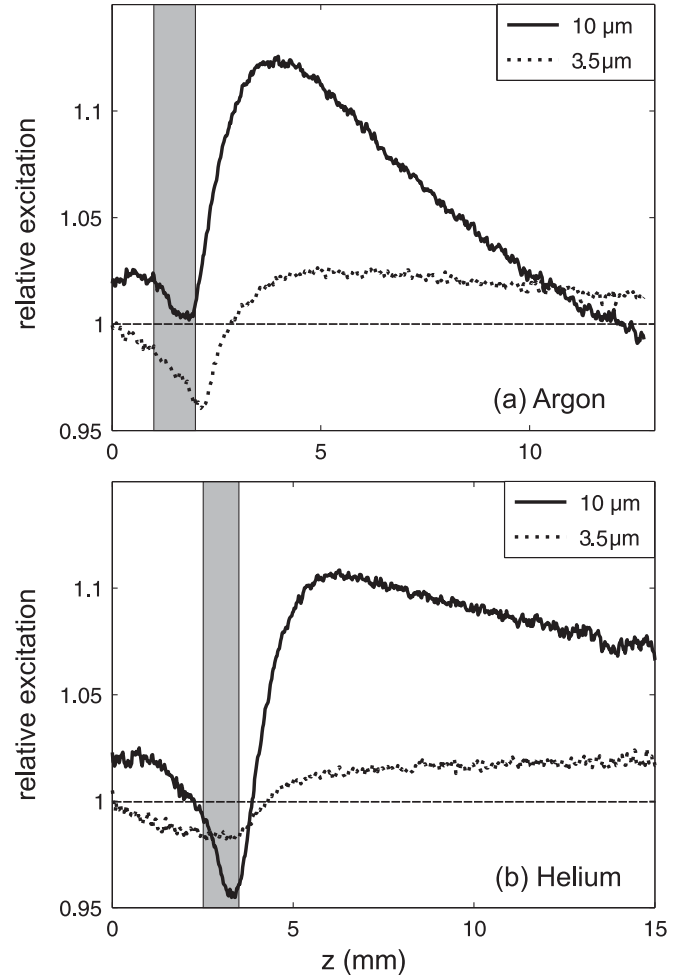


FIG. 7. Time-averaged relative excitation $\bar{X}_{\text{exc}}(z)$ in (a) an argon discharge and (b) a helium discharge versus height above the electrode using dust of 3.5 (dotted line) and 10 μm (solid line) diameter. The shaded areas indicate the height where the dust is trapped.

emission can be expected. In these simulations, it has been observed that the presence of dust leads to an increase of the electron temperature as compared to the dust-free case. (It should be noted, however, that analytical calculations for a dusty DC discharge did not reveal any influence of the dust on the electron distribution function [32].) Land *et al.* [10] determine an increase of electron temperature of about 0.2 eV for a large and dense 3D dust cloud under microgravity conditions. In the void plasma in dusty plasma discharges under microgravity, Klindworth *et al.* [11] observe a temperature increase of up to 0.6 eV. However, these effects have been measured in discharges under microgravity where a large amount of dust is trapped in the plasma.

We also have measured the plasma density and electron temperature in our rf discharge with Langmuir probes similarly to Klindworth *et al.* [33]. In the plasma bulk under the conditions of the experiment, we measured an electron density of $n_{e0} = 1.4 \times 10^{15} \text{ m}^{-3}$ ($n_{ed} = 1.3 \times 10^{15} \text{ m}^{-3}$) without (with) dust trapped in the sheath. The electron temperature was measured as $T_{e0} = 2.4 \text{ eV}$ ($T_{ed} = 2.5 \text{ eV}$). The electron temperature and densities have the same trend as expected from the simulations, but the differences are quite small and

within the error range of the measurements. Hence, modeling is required to reveal the underlying mechanisms.

D. Comparison of different emission lines

To illustrate the behavior of different emission lines, Fig. 8 shows the spatial average of the emission difference in argon for the lines near 750 nm, 810 nm, and 840 nm (see Table I for the respective lines). Hence, the calculated quantity is $\Delta I(t) = \langle I_d(z,t) - I_0(z,t) \rangle_z$, where $\langle \cdot \rangle_z$ indicates averaging over height (at each instant of time t).

A clear temporal modulation of the emission difference $\Delta I(t)$ with the rf cycle (74 ns) is seen for the two lines that are covered by the 750 nm interference filter. The other lines near 810 nm and 840 nm do not show any clear rf modulation. Hence, the above described behavior is most prominently seen for the 750 nm lines.

In a similar manner, the helium 587.5 nm line does not exhibit any strong modulation of $\Delta I(t)$ with the rf period either.

The different behavior of the different lines can be explained as follows: The strongest effects have been observed with the argon lines near 750 nm. Both lines have similar relative intensity and similarly short lifetimes [21]. Furthermore, they end on energy levels ($1s_2$ and $1s_4$, respectively) that are not metastable, and they start from levels $2p_1$ and $2p_5$, which are preferably excited from ground state [26]. This certifies that the emission of these lines is directly affected by the electron dynamics.

In contrast, one of the lines covered by the 810 nm interference filter, namely the 811.5 nm line, is more intense than its counterpart at 810.3 nm by a factor of 2 [21]. More importantly, however, the 811.5 nm line ends on a metastable level ($1s_5$) and is mainly populated through this metastable state [26]. Hence, due to the long lifetime of metastable states, these lines do not exhibit strong modulation differences with the rf cycle.

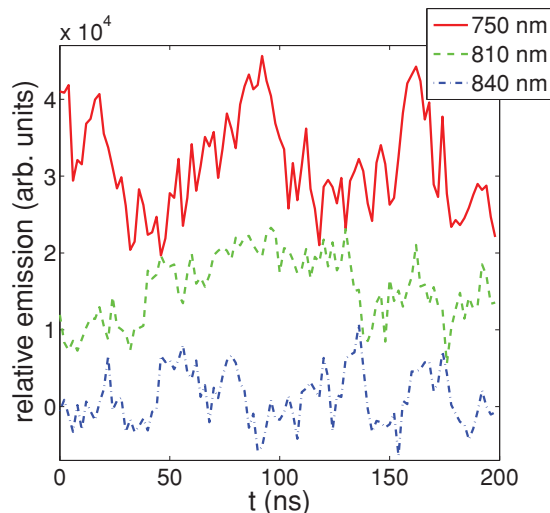


FIG. 8. (Color online) Spatially averaged emission difference $\Delta I(t)$ as a function of time for the different argon lines at 750 nm, 810 nm, and 840 nm.

The two lines near 840 nm have relatively long lifetimes (around 45 ns) which is quite a large fraction of the rf period. They do not end on metastable states. However, these $2p_3$ and $2p_8$ levels are populated only partly by ground state excitation and mostly experience excitation from the metastable levels [26]. Therefore, we did not observe strong excitation differences with and without dust.

In helium, the two investigated lines correspond to equivalent transitions in the singlet and the triplet system. We would thus expect similar behavior of the two lines. Compared to the argon lines, both helium lines have short lifetimes. However, the lifetime of the singlet 667.8 nm line is shorter than the triplet 587.5 nm line by a factor of about 2. Moreover, the intensities of the recorded triplet 587.5 nm line were comparably small and, consequently, the emission profiles were quite noisy. The combination of these effects might result in unobserved excitation differences with and without dust for this particular line.

V. MODELING RESULTS

Now, the P³M code was used to model the phase-resolved emission of dusty rf discharges. The emission has been calculated for the argon 750.4 nm line since, as discussed, it is predominantly populated from ground state excitation and it has shown the strongest effects in the experiment.

In the following, to smooth out fast fluctuations and to have reasonable statistics, averages were taken over 6000 cycles. These averages were taken at fixed rf phases. For convenience, the rf period was split into 65 equally distant phases. Hence, the time resolution is restricted to the time of such a phase frame.

A. Dust charging

The charge is a dynamic property and its dynamics will be studied in the following. The charge results from the balance of the incident fluxes of electrons and ions, for which a phase-resolved study is needed.

Initially, electron fluxes to the dust dominate, leading to the rapid accumulation of a negative dust charge. The charged particle repels further electrons and attracts ions until in equilibrium both electron and ion currents balance on average. This dynamic process of dust charging was already shown in a previous paper [17]. The simulation resulted in an average dust charge of about $-12\,800$ elementary charges. This corresponds to an average floating potential of -3.1 V.

Here, we now resolve the temporal behavior of particle charging within the rf. Figure 9(a) shows the phase of the applied voltage at the lower electrode, which is used in all subsequent plots. In Figs. 9(b) and 9(c) average fluxes of electrons and ions to the dust are shown. The currents are averaged for each of the 65 frames of the phases. These fluxes are multiplied by the time of a single rf phase frame (1.12 ns), yielding the changes in charge, which are then normalized to the average charge q_{dust} in order to compare the magnitude of the charge change $\Delta q/q_{\text{dust}}$ with the analytical results in [34].

As a consequence of the large inertia of ions, the average ion flux to the dust in Fig. 9(b) is nearly constant during the whole rf cycle. Ions get accelerated in the average rf electric field of the sheath to energies of about the average drop of sheath potential and flow constantly to the walls and the dust within the rf.

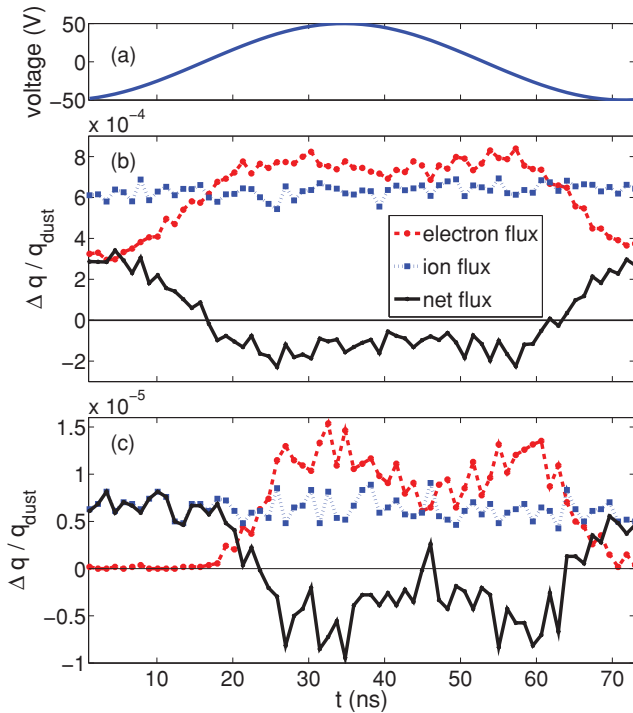


FIG. 9. (Color online) (a) The plot shows the rf voltage at the lower electrode and (b) the simulated phase-resolved, normalized changes in the dust charge according to electron and ion fluxes over rf period to the dust after the transient charging phase. In (c) changes in the dust charge under same conditions as in (b) are shown, except that an artificially decreased collision rate was used.

In contrast to the positive and rather fixed ion background the electrons due to their higher mobility oscillate within the plasma sheath according to the applied rf voltage. Usually, the potential drop in the sheaths near the electrodes results in electric fields directed such that they repel electrons. Only at maximum positive voltage at the rf electrode are the electric fields weak, so that electrons are able to enter the plasma sheath. Hence, the plasma potential rises and falls, driven by the voltage at the rf electrode.

Since electrons are able to react to the rf electric fields in the sheath, the electron flux is modulated. Consequently, the average total charge oscillates with very little amplitude within the rf period. The ratio of net charge change to the total average dust charge $\Delta q / q_{\text{dust}}$ is at maximum 4×10^{-4} . This means that the dust variation of the total average charge of order of 10^4 elementary charges is just a few elementary charges during the rf. According to this variation, also the dust floating potential is actually varying slightly during the rf.

To further illustrate the charging behavior elastic collisions of electrons and ions with neutrals have been switched off in the simulation, shown in Fig. 9(c). Due to the lack of ion-neutral collisions the velocities of the ions are larger. According to ion continuity this yields lower ion densities, which in turn results via Poisson's equation in smaller electric fields, so that the sheath width gets larger to balance fluxes to the wall. As a result, the dust particle is, although at the same place above the electrode, deeper in the plasma sheath. Thus, the electron flux varies more strongly. In the expansion phase the

sheath is completely depleted and thus no electron flux to the dust is observed. With decreasing sheath potential electrons from the tail of the distribution function have enough energy to enter the sheath. Two noticeable maxima in the electron currents are observable. A first peak in the electron flux is seen about 30 ns, when the electrons enter the sheath near the dust. Then, a plateau of nearly constant flux to the dust is achieved, while the electrons are flowing around the dust. Later, the sheath is already building up, and electrons are repelled by electric fields. The flux to the dust is thus forming the second maximum at 55 ns by electrons fleeing from the sheath regions. The removal of elastic collisions reduces the thermalization of the electrons, which results in a more pronounced double-peak structure in Fig. 9(c) compared to Fig. 9(b). The directed flow of electrons in the rf plasma sheaths is thus represented in the microscopic charging dynamics. However, the magnitude of the rf variation decreased to $\approx 10^{-5}$.

A similar oscillation of the charging was analytically calculated [34]. There, dust charge and potential were obtained from fluxes according to collisionless OML theory. The fluctuation of the dust charge induced by the rf resulted from the local electron density, which is given by a Boltzmann term, in which the potential was obtained from the solution of Poisson's equation with a harmonic voltage applied to the rf electrode. In contrast to our results in [34] the dust was placed closer to the presheath. The amplitude of the rf modulation was larger ($\approx 7 \times 10^{-3}$) compared to our findings.

A comparison of the fluxes for the different conditions shows that the currents and with them the variation of the charge decrease toward the wall. The largest flux ratios of electrons to ions have been found close to the presheath in such plasmas [35]. As a result, the magnitude of the fluctuation reduces about an order of magnitude from the case in [34] Fig. 9(b) and further from Fig. 9(b) to Fig. 9(c).

Due to the discreteness of plasma particles, charging is a stochastic process. The fluxes resemble a sequence of discrete absorption events by the grain's surface. Therefore, a fluctuation of the fluxes in Fig. 9 is seen and averaging is required. This stochastic fluctuation corresponds to a standard deviation of the real charge of about 70 elementary charges, which is much larger than the modulation by the rf. The stochastic variation of the charge is consistent with theories [36–39]. Cui and Goree for instance simulated the charge fluctuations based on OML theory. Their fluctuations $\sigma_q \approx 0.5 \sqrt{q_{\text{dust}}} \approx 60$ scale as in the statistics of the counting independent events.

B. Influence of the dust on the CCRF plasma

Here, we model the excitation profiles with and without dust using our P³M code. In the discharge, some electrons gain enough kinetic energy in the rf electric fields during sheath expansion to excite neutrals to higher energetic states. The minimum threshold energy for the excitation from ground state to the excited state $2p_1$ is 13.47 eV, much higher than the thermal energy in low-temperature plasmas, which is of the order of a few eV.

At intermediate pressures (a few tens of Pa) the mean free path of inelastic ($\lambda_{e-n}^* \sim 2$ mm) and elastic collisions ($\lambda_{e-n} \sim 800$ μm) between argon neutrals and electrons is much smaller

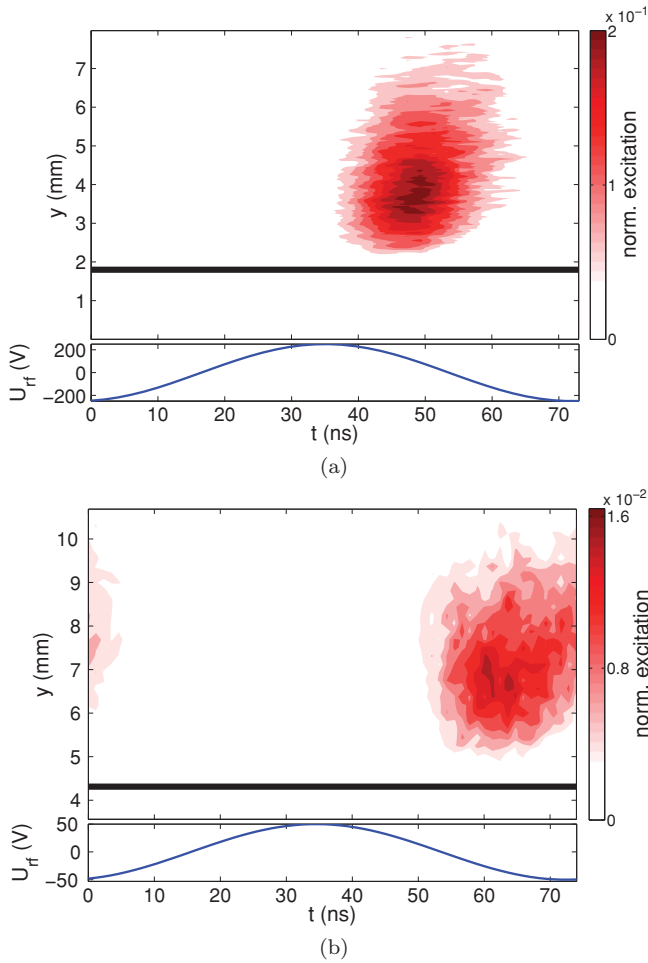


FIG. 10. (Color online) (a) Spatiotemporally resolved excitation difference determined from experimental data of the 750.4 nm spectral line of argon [compare Fig. (5)] and (b) from the simulation. The difference in excitation was calculated by subtracting from the pattern with dust the excitation without dust normalized to the reference without dust. The horizontal solid black line indicates the position of the dust grain; parameters of the experiment $U = 250$ V, $p = 30$ Pa and of the simulation $p = 50$ Pa, $U_{rf} = 50$ V.

than the system length $L = 24$ mm. The kinetic energy of the electrons is either quickly distributed by elastic collisions or transferred to argon neutrals via excitation of higher bound states or even ionization, thus restricting the excitation close to the plasma sheath.

To elucidate the origin of the increase in excitation, corresponding simulations with a single dust particle have been performed. With the dust added to the plasma the excitation profile is similar to the dust-free case. Figure 10 shows the difference in the excitation patterns of the discharge with and without dust of the simulation and the experiment. Both plots are normalized to the dust-free case as a reference. Observable differences of the pattern in time between experiment and simulation are due to different amplitudes of applied voltages. Excitation occurs earlier in the experiment. The stronger the amplitude of the voltage the steeper are the gradients in the potential, so that a certain gain of energy is achieved at earlier phases of the cycle.

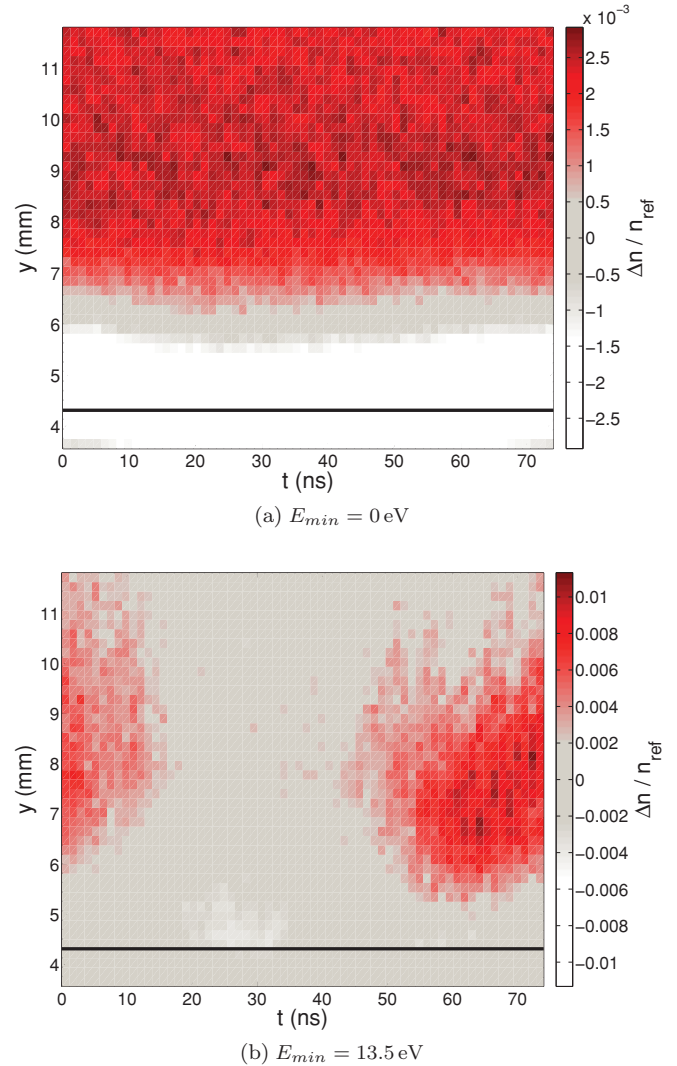


FIG. 11. (Color online) Phase-resolved difference in electron density. Only particles with a higher energy than the indicated energy threshold are counted for the density. The horizontal solid black line indicates dust particle position.

A dust particle added to the simulation increased the excitation above its position during sheath expansion phase. Figure 10(b) shows the results from the P³M simulation. The spatiotemporal behavior qualitatively matches the experimental results in Fig. 10(a). Both the experiment and the simulation agree on the duration of the enhanced excitation (red areas), roughly 25 ns, and its spatial extensions. Maximum excitation occurs 2 mm above the dust, but a significant increase of excitation exists up to 6 mm above the dust. In the simulation the difference in excitation shows a similar pattern as in the experiment. Because of the different amplitudes of the voltage the relative position of the maximum excitation appears at a later instant in time compared to the experiment. In the experiment emission of a plasma with many dust particles in an optical thin plasma was recorded, yielding a larger dust effect in the line of sight. For this reason, the order of magnitude of the normalized difference in the simulation is about a factor of 10 smaller than in the experiment.

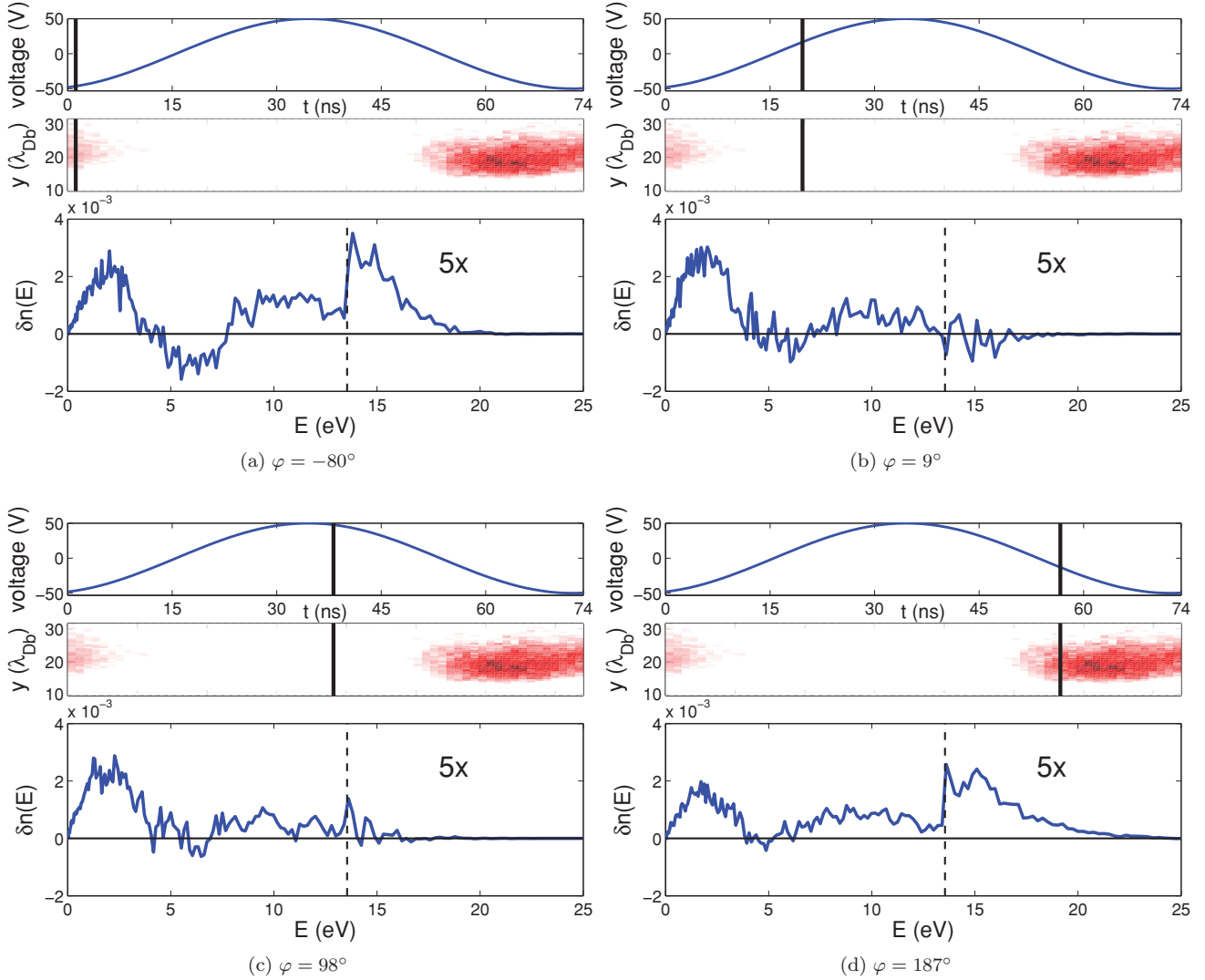


FIG. 12. (Color online) Normalized differences of the time-averaged integral EEDF $\delta n(E) = n_{e,dust}(E) - n_{e,ref}(E)$. The top plot shows the phase and the middle plot the difference in excitation. The vertical solid black line in these plots indicates the phase of the rf cycle. At the bottom the EEDF is plotted. For convenience, the EEDF is summed up over the whole axial extent of the difference in excitation. Indicated by the vertical dashed black line is the energy threshold for excitation from ground state to $2p_1$ at 13.47 eV. From this energy on the density difference is magnified five times.

To analyze the origin of the enhanced excitation the differences in electron density for a plasma with and without dust are presented in Fig. 11. Particle densities are discriminated by the minimum particle energy. Only electrons with a higher energy than energy threshold, 0 eV and 13.5 eV, respectively, were counted for the density. In Fig. 11(a) the density is hardly modulated when electrons with all energies are considered. Bulk electrons at thermal energies are decisive. Since they are not able to enter the sheath, they are thermalized by collisions. Their mere number hides the fluctuation in the density. Toward the dust a decrease in density can be observed, caused by the repulsion of electrons in the dust potential. For a high energy threshold the profiles resemble the spatiotemporal patterns of the excitation. The higher the minimum threshold energy is, the more the density resembles the excitation pattern. The cross sections of the electron impact excitation act as a high pass for

the energies in Eq. (1), thus determining the spatiotemporal pattern of the excitation in low-temperature plasmas.

To investigate further the origin of the increased excitation during sheath expansion the difference of the electron energy distribution function (EEDF) from the case with a dust particle to the case without is shown in Fig. 12. For different rf phases the code was able to resolve this small, higher order effect of the dust to increase the excitation. The difference between the EEDF with dust and without dust for each phase frame is summed up over the concerned spatial range ($y = 5.2\text{--}10\text{ mm}$) where the difference in excitation occurs in order to improve the statistics. We mention that we are investigating the differences in the tail of the electron distribution functions. The difference between the EEDF with dust and without dust is normalized to the maximum value of the EEDF without dust as a reference. Generally, the effect of the dust on the density

per energy in Fig. 12 is small, of the order of $\sim 10^{-3}$ relative to the overall density.

In addition to the sheath potential dynamics, the nearly constant dust potential slightly influences the electrons as well. The dust potential behaves like a small obstacle for electrons in front of the electrode. As a result, electrons whose trajectories intersect with the dip in the plasma potential caused by the dust are on average deflected.

The simulation showed an elevated density of electrons in the energy range 0–4 eV and 8–12 eV in the region between dust and plasma bulk due to the influence of the dust.

During the collapsing phase of the sheath [see Figs. 12(b) and 12(c)] highly energetic electrons are entering the sheath. If they approach the dust, they might interact with the dust potential. Electrons with low kinetic energies (up to 4 eV) are reflected at the dust potential (3.1 V), additionally shielding the bulk electrons from the plasma sheath region, leading to a larger number of electrons in front of the dust toward the plasma bulk. Likewise, during the expansion phase the populations of electrons with energies above 8 eV are enhanced [see Figs. 12(a) and 12(d)], when the dust particle is immersed.

The increased number of particles with high kinetic energies (above 8 eV) can be understood with the following picture: In the expansion phase particles get accelerated by strong electric fields in the sheath. Near the dust the electron motion is impeded by the dust potential, not only during sheath collapse, but also in the expansion phase. Electrons on average are held in the potential well between electrode and dust. Larger electric fields are needed to push the electrons from the plasma sheath. Hence, electrons are released later at higher sheath potential gradients, resulting in stronger accelerations and thus higher kinetic energies. The larger populations of highly energetic electrons seen in Fig. 12 then result in higher excitation rates. The energy gained by the electrons in the electric field of the sheath is then distributed by successive, elastic collisions with neutrals among the degrees of freedom.

At the vertical dashed line the threshold energy for the excitation from ground state to the excited state $2p_1$ at 13.47 eV is indicated. To account for the small amount of the difference in excitation the difference in the EEDF is amplified by a factor of 5. The temporal increase of particles with energies above this threshold fits the enhanced excitation at these phases.

This increase is at the expense of a diminished number of particles of about 5 eV to 6 eV during maximum sheath extent. Particles are held in the vicinity of the dust, so that they are lost for the region where the excitation occurs.

VI. SUMMARY

The phase-resolved excitation of specific atomic emission lines of argon and helium in rf discharges has been measured with and without dust trapped in the space charge region of the sheath. It is found that the excitation in the bulk plasma is enhanced in the dusty discharge with respect to the pure discharge, whereas in the sheath it is slightly reduced. In argon, the observed effects are strongest for the 750 nm lines which have the shortest lifetimes and are preferably excited from ground state. Lines with long lifetimes and/or those populated through metastable states did not show a significant modulation by the dust. In helium, the singlet 667.8 nm line shows similar behavior to that of the 750 nm argon lines, whereas the triplet 587.5 nm line is not as suited to follow the dust modulation as the singlet line.

For a better understanding of the basic physics, the rf dynamics of a dusty CCRF discharge has been resolved with the P³M code. The effects of particle charging and the change in the plasma dynamics, specifically the emission, within the rf are accessible with this model. The oscillating flux of electrons has shown very little variation on the dust charge during the rf cycle. Charge and correspondingly floating potential of the dust were resolved, but showed only very small variations within the rf. Random fluctuations due to the discrete nature of the charging currents are by far more important.

The simulation has shown an increase in the excitation rate when a dust particle is immersed into the plasma as observed experimentally. The simulation identifies the origin of this effect by high energy electrons. The dip in the plasma potential caused by the dust acts as a small obstacle for the electron motion. Not only the dust potential reflects low energy electrons back to the bulk during sheath collapse, but holds back electrons, when the sheath is expanding. These electrons are released from the dust potential well later during the rf cycle, experiencing a larger sheath potential drop and thus gaining higher energies. As a result, electrons are populated at higher energies, so that a small increase in excitation is observed.

ACKNOWLEDGMENTS

Financial support by the Deutsche Forschungsgemeinschaft via SFB-TR24 Grant No. A3 and by the German Aerospace Center DLR under Contract No. 50 WM 0738 is gratefully acknowledged. K.M. and R.S. acknowledge funding by the German Space Agency through Project No. RS0804.

[1] P. K. Shukla and A. A. Mamun, *Introduction to Dusty Plasma Physics* (Institute of Physics Publishing, Bristol, 2002).
 [2] A. Piel and A. Melzer, *Plasma Phys. Controlled Fusion* **44**, R1 (2002).
 [3] V. E. Fortov, A. V. Ivlev, S. A. Khrapak, A. G. Khrapak, and G. E. Morfill, *Phys. Rep.* **421**, 1 (2005).
 [4] O. Havnes, C. K. Goertz, G. E. Morfill, E. Grün, and W. Ip, *J. Geophys. Res.* **92**, 2281 (1987).
 [5] A. Barkan, N. D'Angelo, and R. L. Merlino, *Phys. Rev. Lett.* **73**, 3093 (1994).

[6] P. Belenguer, J. P. Blondeau, L. Boufendi, M. Toogood, A. Plain, A. Bouchoule, C. Laure, and J. P. Boeuf, *Phys. Rev. A* **46**, 7923 (1992).
 [7] A. Bouchoule and L. Boufendi, *Plasma Sources Sci. Technol.* **3**, 292 (1994).
 [8] S. Ratynskaia, M. De Angeli, U. de Angelis, C. Marmolino, G. Capobianco, M. Lontano, E. Lazzaro, G. E. Morfill, and G. Gervasini, *Phys. Rev. Lett.* **99**, 075002 (2007).
 [9] M. R. Akdim and W. J. Goedheer, *Phys. Rev. E* **67**, 056405 (2003).

- [10] V. Land and W. J. Goedheer, *New J. Phys.* **9**, 246 (2007).
- [11] M. Klindworth, O. Arp, and A. Piel, *Rev. Sci. Instrum.* **78**, 033502 (2007).
- [12] S. Mitic, M. Y. Pustynnik, and G. E. Morfill, *New J. Phys.* **11**, 083020 (2009).
- [13] H. T. Do, H. Kersten, and R. Hippler, *New J. Phys.* **10**, 053010 (2008).
- [14] S. Hübner and A. Melzer, *Phys. Rev. Lett.* **102**, 215001 (2009).
- [15] K. Matyash, Ph.D. thesis, Ernst-Moritz-Arndt-Universität, Greifswald, 2003.
- [16] K. Matyash and R. Schneider, *J. Plasma Phys.* **72**, 809 (2006).
- [17] K. Matyash, R. Schneider, F. Taccogna, and D. Tskhakaya, *J. Nucl. Mater.* **363–365**, 458 (2007).
- [18] T. Gans, V. S. von der Gathen, and H. F. Düobebe, *Contrib. Plasma Phys.* **44**, 523 (2004).
- [19] K. Dittmann, D. Drozdov, B. Krames, and J. Meichsner, *J. Phys. D* **40**, 6593 (2007).
- [20] J. Schulze, E. Schüngel, Z. Donko, D. Luggenhölscher, and U. Czarnetzki, *J. Phys. D* **43**, 124016 (2010).
- [21] Y. Ralchenko, A. E. Kramida, J. Reader, and the NIST ASD Team, NIST Atomic Spectra Database (Ver. 2), [<http://www.nist.gov/physlab/data/asd.cfm>].
- [22] J. B. Boffard, R. O. Jung, C. C. Lin, and A. E. Wendt, *Plasma Sources Sci. Technol.* **18**, 035017 (2009).
- [23] K. Matyash, R. Schneider, K. Dittmann, J. Meichsner, F. X. Bronold, and D. Tskhakaya, *J. Phys. D* **40**, 6601 (2007).
- [24] K. Dittmann, Ph.D. thesis, Ernst-Moritz-Arndt-Universität, Greifswald, 2009.
- [25] C. K. Birdsall and A. B. Langdon, *Plasma Physics via Computer Simulation* (McGraw-Hill, Inc., New York, NY, USA, 1985).
- [26] J. B. Boffard, G. A. Piech, M. F. Gehrke, L. W. Anderson, and C. C. Lin, *Phys. Rev. A* **59**, 2749 (1999).
- [27] Á. Yanguas-Gil, J. Cotrino, and L. L. Alves, *J. Phys. D* **38**, 1588 (2005).
- [28] J. E. Chilton, J. B. Boffard, R. S. Schappe, and C. C. Lin, *Phys. Rev. A* **57**, 267 (1998).
- [29] F. Tochikubo, T. Kokubo, S. Kakuta, A. Suzuki, and T. Makabe, *J. Phys. D* **23**, 1184 (1990).
- [30] T. Makabe, N. Nakano, and Y. Yamaguchi, *Phys. Rev. A* **45**, 2520 (1992).
- [31] N. Mutsukura, K. Kobayashi, and Y. Machi, *J. Appl. Phys.* **66**, 4688 (1989).
- [32] G. I. Sukhinin and A. V. Fedoseev, *Phys. Rev. E* **81**, 016402 (2010).
- [33] M. Klindworth Ph.D. thesis, Christian-Albrechts-Universität, Kiel, 2004.
- [34] T. Nitter, *Plasma Sources Sci. Technol.* **5**, 93 (1996).
- [35] V. R. Ikkurthi, K. Matyash, A. Melzer, and R. Schneider, *Phys. Plasmas* **15**, 123704 (2008).
- [36] S. A. Khrapak, G. E. Morfill, A. G. Khrapak, and L. G. D’Yachkov, *Phys. Plasmas* **13**, 052114 (2006).
- [37] T. Matsoukas and M. Russell, *J. Appl. Phys.* **77**, 4285 (1995).
- [38] T. Matsoukas, M. Russell, and M. Smith, *J. Vac. Sci. Technol. A* **14**, 624 (1996).
- [39] C. Cui and J. Goree, *IEEE Trans. Plasma Sci.* **22**, 151 (1994).